



## Co-delivery of erlotinib and doxorubicin by pH-sensitive charge conversion nanocarrier for synergistic therapy



Yongju He<sup>a</sup>, Zhigui Su<sup>b</sup>, Lingjing Xue<sup>b</sup>, Hui Xu<sup>a,b,\*</sup>, Can Zhang<sup>b,\*\*</sup>

<sup>a</sup> Lab of Nano-biology Technology, School of Physics and Electronics, Central South University, Changsha, Hunan 410083, China

<sup>b</sup> State Key Laboratory of Natural Medicines, Jiangsu Key Laboratory of Drug Discovery for Metabolic Diseases, China Pharmaceutical University, Nanjing 210009, China

### ARTICLE INFO

#### Article history:

Received 3 December 2015

Received in revised form 4 February 2016

Accepted 1 March 2016

Available online 3 March 2016

#### Keywords:

pH-sensitive

Charge conversion

MSN

Erlotinib

DOX

Synergistic therapy

### ABSTRACT

Pretreatment of lung cancer cells with epidermal growth factor receptor (EGFR) inhibitor erlotinib has been recently reported that could dramatically synergize their apoptotic response to DNA damage agent doxorubicin (DOX). To translate this synergistic therapy into *in vivo* anticancer therapy and clinical practice, we designed a novel pH-sensitive charge conversion nanocarrier (M-HHG<sub>2</sub>C<sub>18</sub>-L) that contained erlotinib/DOX combination and produced a sequential staggered drug release for synergistic lung cancer therapy. In this study, a synthetic zwitterionic oligopeptide lipid (1,5-dioctadecyl-L-glutamyl2-histidyl-hexahydrobenzoic acid, HHG<sub>2</sub>C<sub>18</sub>) was used to construct a pH-sensitive lipid bilayer (HHG<sub>2</sub>C<sub>18</sub>-L), which was subsequently applied to coat amino-functionalized mesoporous silica nanoparticles (MSN-NH<sub>2</sub>). Erlotinib and DOX were separately incorporated into HHG<sub>2</sub>C<sub>18</sub>-L and MSN-NH<sub>2</sub> respectively to obtain pH-sensitive charge conversion erlotinib/DOX co-delivery nanoparticles (M-HHG<sub>2</sub>C<sub>18</sub>-L(E + D)). We confirmed that M-HHG<sub>2</sub>C<sub>18</sub>-L(E + D) were able to reverse surface zeta potential from negative to positive at tumor extracellular pH, thus facilitating the targeted cancer cell internalization. Furthermore, as erlotinib was sequestered in the exterior lipid bilayer and the controlled release ability of MSN-NH<sub>2</sub>, erlotinib released faster than DOX during the cellular transport. Additionally, HHG<sub>2</sub>C<sub>18</sub>-L became more positive at tumor intracellular pH and enhanced Coulombic repulsion with MSN-NH<sub>2</sub>, leading to increased sequential staggered release of erlotinib and DOX. Due to the pretreatment and time-staggered inhibition of EGFR with erlotinib and the enhanced intracellular release of DOX to the nucleus, the maximized synergistic cell killing effect was achieved. Compared to non-sensitive erlotinib/DOX co-delivery nanoparticles (M-SPC-L(E + D)) and simultaneous DRUG coadministration, M-HHG<sub>2</sub>C<sub>18</sub>-L(E + D) with sequential staggered drug release and pH-sensitive charge conversion properties showed great synergistic effects in antiproliferation and apoptosis of A549 human cancer cells *in vitro*. The *in vivo* study demonstrated that M-HHG<sub>2</sub>C<sub>18</sub>-L(E + D) exhibited considerable tumor accumulation and potent suppression of tumor growth in Lewis lung carcinoma tumor bearing mice. It was also demonstrated that M-HHG<sub>2</sub>C<sub>18</sub>-L(E + D) showed no systemic toxicity and possessed distinguished effect on extending survival period. These results suggested that M-HHG<sub>2</sub>C<sub>18</sub>-L(E + D) had great potential application in cancer treatment.

© 2016 Elsevier B.V. All rights reserved.

### 1. Introduction

Cancer is now the leading cause of deaths in the world [1,2] and will lead to millions of people dying between 2005 and 2015 estimated by the World Health Organization [3]. Chemotherapy or radiation therapy, which functions by damaging DNA in cancerous cells is the mostly common option in cancer treatment [4], but it causes many undesired effects, primarily because of its inefficiency in tumor-targeting and toxic effects on healthy tissue [5,6]. It was important to develop potent therapeutic strategies which can enhance cancer therapy. Recent drug

screening efforts focused on careful selection of drug cocktails [7–14]. Lee et al. [15] reported that pretreatment of lung cancer cells with epidermal growth factor receptor (EGFR) inhibitor erlotinib could remarkably synergize their apoptotic response to DNA damage agent doxorubicin (DOX). This work indicated the importance of a specific time lag between the administration of each drug for maximizing the synergistic effects of combination chemotherapy. However, the different pharmacokinetic parameters for each drug, poor penetration and distribution in solid tumors bring difficulties in targeting both drugs to the same tumor cells and limit their adequacy as chemotherapeutic agents *in vivo* [16,17]. To address these challenges, Morton et al. [18] used folate-functionalized liposome as delivery platform capable to achieve intracellular co-localization of both drugs and time-staggered release of the synergistic erlotinib/DOX. However, such a single liposome could not control the sequence release of drugs precisely. Besides,

\* Corresponding author at: Lab of Nano-biology Technology, School of Physics and Electronics, Central South University, Changsha, Hunan 410083, China.

\*\* Corresponding author.

E-mail addresses: [xuhui@csu.edu.cn](mailto:xuhui@csu.edu.cn) (H. Xu), [zhangcan@cpu.edu.cn](mailto:zhangcan@cpu.edu.cn) (C. Zhang).

compared with the strategy of active targeting ligand decoration, the nanosystems using the tumor pH for enhanced cellular internalization are easy to prepare and can be exploited for the treatment of all kinds of tumor [19,20]. Additionally, the targeting of tumor extracellular pH ( $pH_e$ , pH 6.0–7.0) is insensitive to protein heterogeneity and is also not limited by the numbers of biomarkers on the cell surface [21].

Herein, we applied pH-sensitive lipid bilayer (HHG<sub>2</sub>C<sub>18</sub>-L) to coat amino-functionalized mesoporous silica nanoparticles (MSN-NH<sub>2</sub>) to construct a pH-sensitive charge conversion nanocarrier (M-HHG<sub>2</sub>C<sub>18</sub>-L) for lung cancer therapy. Erlotinib and DOX were separately incorporated into HHG<sub>2</sub>C<sub>18</sub>-L and MSN-NH<sub>2</sub> to obtain pH-sensitive charge conversion erlotinib/DOX co-delivery nanoparticles (M-HHG<sub>2</sub>C<sub>18</sub>-L(E + D)). Functional HHG<sub>2</sub>C<sub>18</sub>-L contained 1,5-dioctadecyl-L-glutamyl 2-histidyl-hexahydrobenzoic acid (HHG<sub>2</sub>C<sub>18</sub>) presented negative charge in the physiological environment, and reversed from negative to positive irritated by  $pH_e$  [22]. Due to the proton sponge effect of the imidazole group of histidine in HHG<sub>2</sub>C<sub>18</sub>, M-HHG<sub>2</sub>C<sub>18</sub>-L(E + D) could escape from the endosomes/lysosomes. Also, hexahydrobenzoic amide hydrolyses triggered by tumor intracellular pH ( $pH_i$ , pH 4.0–6.0) provided the HHG<sub>2</sub>C<sub>18</sub>-L with a stronger positive charge by the loss of carboxyl groups in HHG<sub>2</sub>C<sub>18</sub> [22]. While

MSN-NH<sub>2</sub>, on the one hand played an essential role to slow the release rate of the incorporated DOX to guarantee a specific time lag between the release of DOX and erlotinib because of its strong interaction with DOX, on the other hand enhanced the subsequently time-staggered drug release by Coulombic repulsion with positive HHG<sub>2</sub>C<sub>18</sub>-L at  $pH_i$ . M-HHG<sub>2</sub>C<sub>18</sub>-L(E + D) presented a shell first, core second feature to produce the sequential and time-staggered drug release, which was critical to maximize the synergistic effects of drug combination.

As depicted in Fig. 1, once accumulated in tumor site through enhanced permeability and retention effect (EPR) [23,24], M-HHG<sub>2</sub>C<sub>18</sub>-L(E + D) reversed surface charge from negative to positive under extracellular pH to facilitate cell uptake. After entering into the cells, as erlotinib was sequestered in the exterior lipid bilayer and the controlled release ability of MSN-NH<sub>2</sub>, erlotinib would release faster than DOX. Additionally, HHG<sub>2</sub>C<sub>18</sub>-L was more positively charged in intracellular pH and induced a strong Coulombic repulsion with MSN-NH<sub>2</sub>, leading to destabilized state between HHG<sub>2</sub>C<sub>18</sub>-L and MSN-NH<sub>2</sub>, as a result, increasing sequential staggered release of erlotinib and DOX, which inhibited kinase domain of EGFR in cell membrane and targeted to nucleus respectively. Since the pretreatment and time-staggered inhibition of EGFR with erlotinib and the enhanced DOX release to the

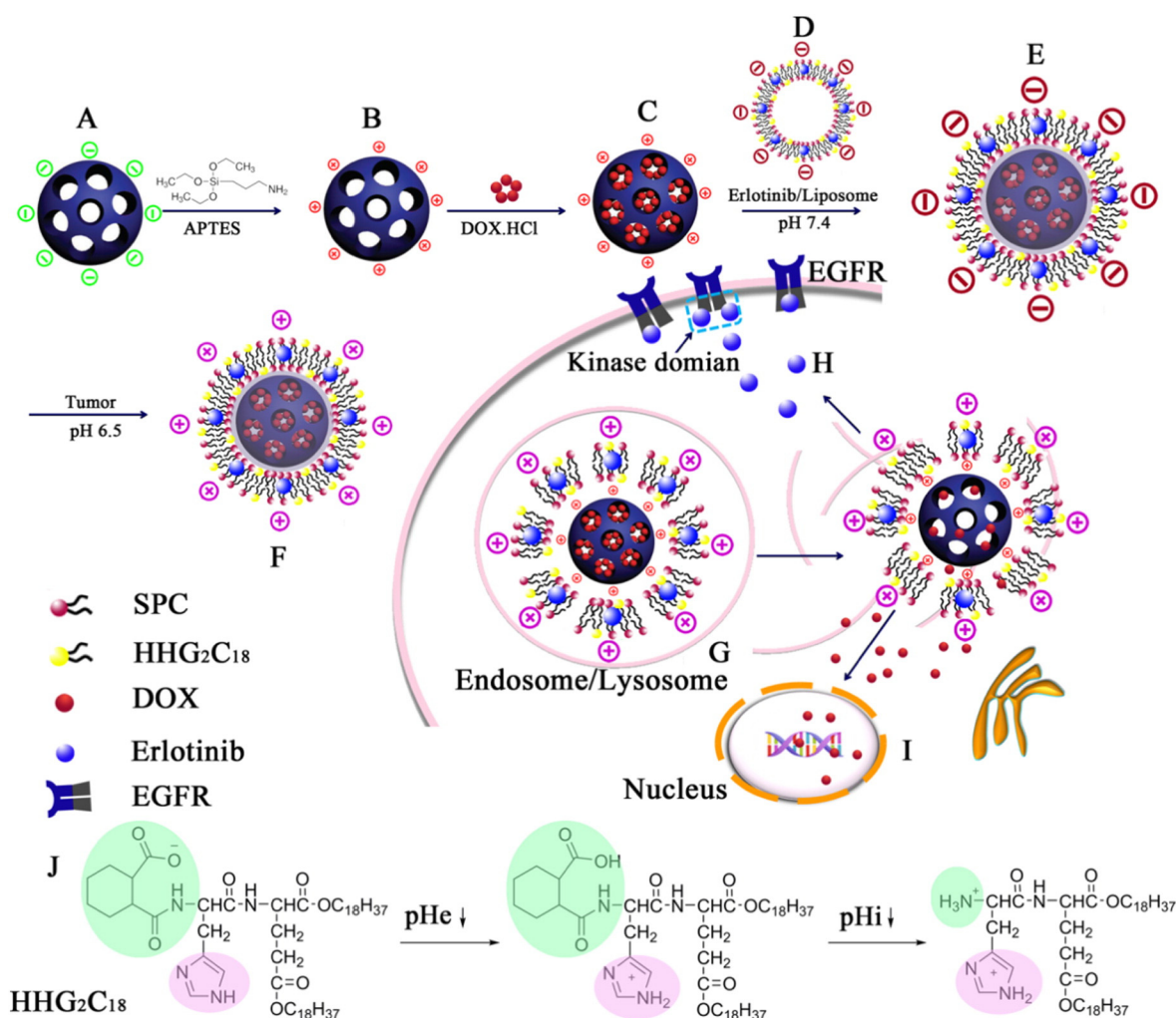


**Fig. 1.** Schematic illustration of preparation of erlotinib/DOX combination co-delivery nanocarriers and synergistic therapy of erlotinib and DOX. The surface of mesoporous silica nanoparticles (A) were modified with 3-aminopropyltriethoxysilane (APTES) to form MSN-NH<sub>2</sub> (B). MSN-NH<sub>2</sub> were then loaded with DOX to obtain DOX-loaded MSN-NH<sub>2</sub> (C), followed by support with erlotinib-loaded lipid bilayer (D) to yield M-HHG<sub>2</sub>C<sub>18</sub>-L(E + D) (E). After injection of M-HHG<sub>2</sub>C<sub>18</sub>-L(E + D), the nanoparticles accumulated at the tumor site through enhanced permeability and retention effect in tumor blood vessels. M-HHG<sub>2</sub>C<sub>18</sub>-L(E + D) were positively charged at extracellular environment (F) leading to easy internalization by tumor cells. After cell uptake, as erlotinib was loaded in the exterior lipid bilayer and the controlled release ability of MSN-NH<sub>2</sub>, erlotinib released faster than DOX. Additionally, the lipid bilayer was more positive and induced a strong repulsion with MSN-NH<sub>2</sub> in intracellular environment (G), enhancing sequential staggered release of erlotinib and DOX, which was pretreated and staggered to inhibit kinase domain of EGFR in cell membrane (H) and was targeted to cell nucleus (I) respectively, thus maximized the synergistic therapy. Effect of extracellular and intracellular pH ( $pH_e$  and  $pH_i$ ), respectively on the HHG<sub>2</sub>C<sub>18</sub> (J).

nucleus, the maximized synergistic therapy against tumor cells was achieved. In this study, the pH-sensitive charge conversion behavior, the in vitro drug release and the cell uptake were investigated in detail. The synergistic antitumor effect of M-HHG<sub>2</sub>C<sub>18</sub>-L(E + D) was extensively evaluated and the results compared with those obtained using simultaneous drugs cotreatment or non-sensitive erlotinib/DOX co-delivery nanoparticles (M-SPC-L(E + D)).

## 2. Materials and methods

### 2.1. Materials

Tetraethyl orthosilicate (TEOS, 98%), ammonium solution (25.00–28.00 wt.%), hydrochloric acid (HCl, 37%) and ethanol were obtained from Fuke Chemical Reagent Co. (Changsha, China). N-octadecyltrimethoxysilane (C<sub>18</sub>TMS, 95%) was purchased from Baxi Chemical Reagent Co. (Changsha, China). 3-Aminopropyltriethoxysilane (APTES) was acquired from Aladdin Industrial Inc. (Shanghai, China). Soy phosphatidylcholine (SPC) was offered by Taiwei Pharmaceutical Co., Ltd. (Shanghai, China). Cholesterol (Chol) was provided by Huixing Biochemical Reagent Co., Ltd. (Shanghai, China). 1, 5-Dioctadecyl-L-glutamyl-2-histidyl-hexahydrobenzoic acid (HHG<sub>2</sub>C<sub>18</sub>) was previously synthesized by our group. Rhodamine-PE, fluorescein isothiocyanate ester (FITC), erlotinib, doxorubicin hydrochloride, chlorpromazine, NaN<sub>3</sub>, amiloride and nystatin were from Sigma-Aldrich Co. (Shanghai, China). RPMI-1640 medium (1640, Hyclone®), Dulbecco's modified Eagle medium (DMEM, Hyclone®), trypsin (Hyclone®), fetal bovine serum (FBS, Hyclone®), penicillin-streptomycin solution (Hyclone®), phosphate buffered saline (PBS, Hyclone®) and 3-(4,5-dimethylthiazol-2-yl)-2,5-diphenyltetrazolium bromide (MTT) were provided by Sunshine Biotechnology Co., Ltd. (Nanjing, China). LysoTracker green was purchased from Life Technologies Co. (Shanghai, China), DAPI and Annexin V-FITC apoptosis detection kit were purchased from Beyotime Institute of Biotechnology (Nantong, China). All other chemicals and reagents were used as received. Deionized water which was prepared with an ion exchange system was used in all experiments.

### 2.2. Synthesis and characterization of mesoporous silica nanoparticles and amino-functionalized mesoporous silica nanoparticles

Mesoporous silica nanoparticles (MSN) were synthesized as described in our previous study [42], and amino-functionalized mesoporous silica nanoparticles (MSN-NH<sub>2</sub>) were synthesized as follows: MSN (275 mg) were dispersed in toluene (60 mL) with vigorous stirring, followed by adding APTES (4.3 mmol) in drops as reaction temperature raised up to 116, and further stirred for 24 h under reflux. Subsequently, the synthesized MSN-NH<sub>2</sub> were collected via centrifuging at 5000 rpm for 5 min, washed by ethanol thrice, and dried overnight at room temperature in vacuum.

The morphology and structure of MSN and MSN-NH<sub>2</sub> were observed via cryogenic transmission electron microscopy (Cryo-TEM, FEI Tecnai G2 20 TWIN) with an accelerating voltage of 200 kV. Surface area, pore volume and pore size distributions of MSN and MSN-NH<sub>2</sub> were measured by nitrogen sorption method which carried out at 77 K on a Micromeritics Thristar 3000 analyzer. The amino groups on the surface of MSN were qualitatively confirmed by the Fourier Transform infrared spectroscopy (FTIR) using a Thermo Scientific Nicolet 6700 FTIR spectrometer (Asheville, NC, USA) and zeta potential using a ZetaPlus Zeta Potential Analyzer (Brookhaven, USA), and quantified by fluorescamine measurements.

### 2.3. Preparation of M-HHG<sub>2</sub>C<sub>18</sub>-L(E + D) and M-SPC-L(E + D)

Using different lipid compositions, we fabricated a pH-sensitive charge conversion lipid film composed of SPC/HHG<sub>2</sub>C<sub>18</sub>/Chol at a weight

ratio of 3.75:1.25:1, while prepared a traditional lipid film with SPC and Chol at a weight ratio of 5:1. 1% (w:w) erlotinib of the total lipids was added to the lipid components to construct the drug-loaded lipid film. These components were dissolved in 5 mL of chloroform in a round-bottom flask. A thin lipid film was formed after the solvent was evaporated under vacuum in a rotary evaporator at 40. These films were continued vacuum drying overnight to eliminate traces of organic solvents.

To achieve DOX loaded MSN-NH<sub>2</sub> (DOX/MSN-NH<sub>2</sub>), DOX were dissolved in deionized water with a concentration of 1 mg/mL, then 60 mg of MSN-NH<sub>2</sub> was soaked in 1.4 mL of DOX solution for 24 h under light-sealed condition. DOX/MSN-NH<sub>2</sub> were collected by centrifugation at 5000 rpm for 5 min, and washed with deionized water repeatedly to remove the excess DOX.

For preparation of synergic erlotinib/DOX co-delivery system, DOX/MSN-NH<sub>2</sub> were ultrasonically dispersed in 5 mL of deionized water and immediately added on top of the erlotinib-containing lipid film occupied at the bottom of flask, followed by hydration at 37 for 15 min to attach a surface lipid bilayer. The dual drug-loaded M-HHG<sub>2</sub>C<sub>18</sub>-L(E + D) or M-SPC-L(E + D) were achieved after centrifugation to remove excess lipid bilayer. The successfully coated lipid bilayer on MSN-NH<sub>2</sub> was evidenced by the changed zeta potential and observed via TEM. The amount of DOX loaded in the nanoparticles was measured by a microplate reader (POLARstar Omega, Germany) with an emission wavelength of 485 nm and emission wavelength of 550 nm. The amount of erlotinib loaded in the nanoparticles was measured by High Performance Liquid Chromatography (HPLC) with mobile phase of acetonitrile/KH<sub>2</sub>PO<sub>4</sub> buffer (6:4, v:v), flow 1 mL min<sup>-1</sup>, detection 345 nm, injected volume 20 μL and C<sub>18</sub> column. The encapsulation efficiency (EE) was calculated according to the following formulas:

$$EE = \frac{W_1}{W_2} \times 100\% \quad (1)$$

where  $W_1$  and  $W_2$  are weight of loaded drug and total amount of feeding drug, respectively.

### 2.4. pH-sensitive charge conversional behavior

The pH-sensitive charge reversal of M-HHG<sub>2</sub>C<sub>18</sub>-L(E + D) was verified by zeta potential analysis at different pH values (pH 7.4, 6.5, 5.5, 4.5). Briefly, M-HHG<sub>2</sub>C<sub>18</sub>-L(E + D) was diluted in different pH buffers, then the zeta potentials were measured at room temperature by a ZetaPlus Zeta Potential Analyzer (Brookhaven, USA).

To further investigate the state between interior MSN-NH<sub>2</sub> and HHG<sub>2</sub>C<sub>18</sub>-L shell at different pH values. FITC and rhodamine B were used to label MSN-NH<sub>2</sub> and HHG<sub>2</sub>C<sub>18</sub>-L respectively to form fluorescent resonance energy transfer M-HHG<sub>2</sub>C<sub>18</sub>-L (referred to as FRET M-HHG<sub>2</sub>C<sub>18</sub>-L), then FRET phenomenon was studied at different pH values. Briefly, FITC was dissolved in ethanol followed by adding MSN-NH<sub>2</sub>. The mixture was stirred overnight in the dark. Finally, MSN-NH<sub>2</sub>-FITC were collected by centrifugation. Rhodamine-PE was added to the mixture of SPC/HHG<sub>2</sub>C<sub>18</sub>/Chol to synthesize rhodamine labeled HHG<sub>2</sub>C<sub>18</sub>-L. FRET M-HHG<sub>2</sub>C<sub>18</sub>-L were obtained by coating rhodamine labeled HHG<sub>2</sub>C<sub>18</sub>-L on MSN-NH<sub>2</sub>-FITC. FRET M-HHG<sub>2</sub>C<sub>18</sub>-L were diluted in different pH buffers (pH 7.4, 6.5, 5.5, 4.5), then the fluorescence emission spectra in the range of 500 to 700 nm were recorded with an excitation wavelength at 485 nm. FRET efficiency can be calculated according to Eq. (2):

$$E_{FRET} = \frac{F_A}{F_A + F_D} \times 100\% \quad (2)$$

where  $F_A$  and  $F_D$  are the fluorescence spectra of acceptor and donor samples respectively.

### 2.5. *In vitro* drug release

The drug release based on erlotinib/DOX formulations were investigated in PBS at different pH values (pH 7.4, 6.5, 5.5, 4.5) by dialysis method. Briefly, 0.5 mL of M-HHG<sub>2</sub>C<sub>18</sub>-L (E + D) and M-SPC-L (E + D) were transferred into a dialysis bag (MWCO 14000 Da) respectively. The bags were then submerged in 25 mL of PBS at 37 °C and shaken at a speed of 100 rpm. At predetermined time intervals, 0.5 mL of release media was extracted to quantitatively analyze the concentration of erlotinib and DOX released respectively, and equal volume of fresh PBS solution was replenished. The concentration of DOX and erlotinib were measured by a microplate reader and HPLC, respectively. The accumulative release percentage (ARP) was calculated by formula:

$$ARP = \frac{A_0}{A} \times 100\% \quad (3)$$

where  $A_0$  is the amount of drug in release medium,  $A$  is the amount of drug loaded into nanoparticles.

### 2.6. Cell culture

Human non-small-cell lung cancer (A549) cells were cultured in RPMI 1640 and Lewis lung carcinoma (LLC) cells were cultured in Dulbecco's modified Eagle medium (DMEM) with high glucose. Both medium supplemented with 10% (v:v) FBS 100 U/mL of penicillin and 100 µg/mL of streptomycin. Cells were maintained in an incubator (Thermo Scientific, USA) at 37 under an atmosphere of 5% CO<sub>2</sub> and 90% relative humidity. Cell concentrations were determined by counting trypsinized cells with a hemocytometer.

### 2.7. Cellular uptake and endocytosis pathway

Human non-small-cell lung cancer (A549) ( $1 \times 10^5$  cells/well) cells were seeded and used for the uptake assays after culturing on 24-well plates under 5% CO<sub>2</sub> at 37 °C for 24 h. To investigate the effect of pH-sensitive charge conversion of M-HHG<sub>2</sub>C<sub>18</sub>-L(E + D) on enhancing tumor cellular uptake at extracellular environment, erlotinib/DOX-loaded carriers including M-HHG<sub>2</sub>C<sub>18</sub>-L(E + D) and M-SPC-L(E + D) were diluted in the FBS-free culture medium at pH 7.4 and pH 6.5 to reach a final DOX concentration of 10 µg/mL, 500 µL per well for 4 h at 37, the medium was removed and the cells were washed by 4 °C PBS thrice to stop the cellular uptake, then 200 µL of cell lysis buffer was added to each well. After incubation at 37 for another 0.5 h, the cells were harvested, the Si element of nanocarriers including M-HHG<sub>2</sub>C<sub>18</sub>-L and M-SPC-L was quantitatively analyzed by Inductively Coupled Plasma/Mass Spectrometer (ICP-OES/ICP-MS, Optima 5300DV, USA), the amounts of erlotinib and DOX were measured quantitatively by a microplate reader and HPLC, respectively.

The real time observation of the cellular internalization process was performed under a confocal laser scanning microscope (CLSM, ZEISS LSM700, Germany). Briefly, A549 cells were seeded in a special confocal microscopy dish with  $1 \times 10^5$  cells/well density in 1 mL of RPMI 1640 and cultured for 24 h at 37, and then the original medium was replaced with FBS-free medium, which including M-HHG<sub>2</sub>C<sub>18</sub>-L(E + D) or M-SPC-L(E + D). The concentration of corresponding DOX was 2 µg/mL and the cells were then incubated for 1 h, 4 h, 8 h and 12 h at 37, respectively. Subsequently, the cells were washed by 4 PBS thrice to remove the residual nanoparticles. Then, 50 nM DAPI was used to stain the nuclei for 15 min at 37. Finally, the cells were washed by PBS thrice and visualized by CLSM. Blue and red luminescent emissions from DAPI and DOX were excited at the wavelength of 405 nm and 488 nm, respectively.

To investigate the endocytotic mechanisms of M-HHG<sub>2</sub>C<sub>18</sub>-L(E + D) and M-SPC-L(E + D), A549 cells were pretreated with various endocytic inhibitors for 30 min. The kinds of inhibitors and their concentrations

were as follows: 133 µg/mL of amiloride (an inhibitor of macropinocytosis), 15 µg/mL of nystatin (an inhibitor of caveolin-mediated endocytosis), 50 µg/mL of chlorpromazine (an inhibitor of clathrin-mediated endocytosis) and 1 mg/mL of NaN<sub>3</sub> (an inhibitor of energy-mediated endocytosis). Subsequently, the inhibitors were removed, uptake study was performed by incubation with M-HHG<sub>2</sub>C<sub>18</sub>-L(E + D) and M-SPC-L(E + D) at DOX concentration of 10 µg/mL for 4 h at 37. Results were expressed as the uptake percentage of control cells that were only incubated with erlotinib/DOX-loaded carriers at 37 for 4 h.

### 2.8. *In vitro* cytotoxicity and cell apoptosis

The cytotoxicity of M-HHG<sub>2</sub>C<sub>18</sub>-L(E + D) was tested in A549 cells. Briefly, A549 cells were seeded at a density of  $5 \times 10^3$  cells/well in 200 µL of RPMI 1640 medium in 96-well plates and grown for 24 h to allow cell attachment. The cells were then incubated with the FBS-free culture medium adjusted to pH 7.4 or pH 6.5 containing M-HHG<sub>2</sub>C<sub>18</sub>-L(E + D) in a concentration gradient at 37 °C for another 24 h. Subsequently, 20 µL of methylthiazolotetrazolium solution (5 mg/mL in phosphate-buffered saline) was added to each well and further incubated for 4 h. After the incubation, the medium in each well was removed, and 200 µL of dimethyl sulfoxide (DMSO) was added to dissolve the internalized purpleformazan crystals at room temperature. Absorbance was measured at 570 nm by a microplate reader (Thermo Scientific, USA). Viability which was estimated from data from six individual experiments was normalized to untreated controls, and the concentration required to achieve 50% inhibition of signal (IC<sub>50</sub>) was calculated. M-SPC-L(E + D), free erlotinib and DOX mixture (F(E + D)), single DOX loaded nanoparticles (M-HHG<sub>2</sub>C<sub>18</sub>-L(D)) and M-HHG<sub>2</sub>C<sub>18</sub>-L(D) plus free erlotinib (M-HHG<sub>2</sub>C<sub>18</sub>-L(D) + E) were used as the comparisions.

To investigate the effect of M-HHG<sub>2</sub>C<sub>18</sub>-L(E + D), M-SPC-L(E + D), F(E + D), M-HHG<sub>2</sub>C<sub>18</sub>-L(D) + E and M-HHG<sub>2</sub>C<sub>18</sub>-L(D) on cell apoptosis, flow cytometry was performed using Annexin V-FITC apoptosis detection kit. Briefly,  $1 \times 10^6$  A549 cells per well were seeded in 12-well plates with 1 mL of complete RPMI 1640 medium for 24 h at 37 °C. The cells were then treated with different formulations at corresponding DOX concentration of 10 µg/mL at pH 7.4 and pH 6.5. Control experiments were performed by adding only culture medium. After 12 h of treatment, the cells were trypsinized and harvested, washed with 4 °C PBS twice and resuspended in 500 µL of binding buffer, then 5 µL of Annexin V-FITC and 5 µL of propidium iodide were added and incubated in the dark for 10 min. The cells were immediately analyzed by BD accuri flow cytometry.

### 2.9. Animals and tumor xenograft models

Male Sprague-Dawley (SD) rats (180–220 g) and male C57/BL6 mice (18–20 g) were purchased from Qinglongshan Co. (Nanjing, China). All animal experiments were carried out in accordance with Institutional Animal Care and Use Committee guidelines.

To set-up the tumor xenograft model, approximately  $5 \times 10^6$  LLC cells suspended in saline (200 µL) were subcutaneously injected into the right flank of C57/BL6 mice. Tumor volume (V) was determined by measuring the largest superficial diameter (a) and the smallest superficial diameter (b), and calculated as  $V = a \times b^2/2$ .

### 2.10. Pharmacokinetics

To determine the pharmacokinetic profiles of M-HHG<sub>2</sub>C<sub>18</sub>-L(E + D), M-SPC-L(E + D) and F(E + D). SD rats (180–220 g) were randomly divided into three groups (n = 6), and received intravenous injection of M-HHG<sub>2</sub>C<sub>18</sub>-L(E + D), M-SPC-L(E + D) and F(E + D) at DOX dose of 5 mg/kg and erlotinib dose of 1.92 mg/kg. At the time point of 0.083 h, 0.167 h, 0.25 h, 0.5 h, 1 h, 2 h, 4 h, 6 h, 8 h, 12 h and 24 h

following injection, blood samples were collected and then stored at  $-20\text{ }^{\circ}\text{C}$  until microplate reader and HPLC analysis.

The pharmacokinetic parameters of erlotinib and DOX formulations, such as the maximum plasma concentration ( $C_{\text{max}}$ ), the area under the plasma concentration-time curve (AUC), the plasma elimination half-life ( $T_{1/2}$ ) and mean residence time (MRT) were obtained using a non-compartmental model by Kinetica 4.4 (Thermo, USA).

### 2.11. Biodistribution

The *in vivo* imaging system was used to study the biodistribution of DIR-labeled M-HH<sub>2</sub>C<sub>18</sub>-L and M-SPC-L in the LLC subcutaneous xenograft model in C57/BL6 mice. The mice were observed at the predetermined time (1 h, 4 h, 6 h, 8 h, 12 h and 24 h) after intravenous injection DIR-labeled M-HH<sub>2</sub>C<sub>18</sub>-L or M-SPC-L at DIR dose of 0.4 mg/kg into the tumor-bearing mice. At the end of the experiment, the animals were sacrificed and tumor tissues as well as major organs (heart, kidney, liver, lung and spleen) were collected, weighed, and observed with the *in vivo* imaging system. Tumor tissue slices were stained with DAPI and observed by CLSM (ZEISS LSM700, Germany).

### 2.12. Antitumor efficacy *in vivo*

5 days after tumor implantation, LLC tumor-bearing mice were weighed and randomized into six groups (12 mice per group), and received M-HH<sub>2</sub>C<sub>18</sub>-L(E + D), M-SPC-L(E + D), F(E + D), M-HH<sub>2</sub>C<sub>18</sub>-L(D) + E and M-HH<sub>2</sub>C<sub>18</sub>-L(D) at DOX dose of 2 mg/kg and erlotinib dose of 0.77 mg/kg through tail vein injection for every other days with a total of five doses. Control mice received the same volume of saline. The tumor-bearing mice were weighted and tumor sizes were measured every day to evaluate the antitumor activities and systemic toxicity. At day 17 post-tumor inoculation, some mice

were sacrificed by cervical vertebra dislocation. The tumors and major organs, including heart, liver, spleen, lung and kidney were harvested and sectioned for histopathology analyses with hematoxylin and eosin (H&E) staining. The cell apoptosis of tumor tissue was also detected by TUNEL staining according to the manufacturer's protocol. The remaining mice were used for survival analysis.

### 2.13. Statistical analysis

Quantitative data are presented as mean  $\pm$  standard deviation (SD). Statistical comparisons between different treatments were analyzed by the Student's *t*-test or one-way ANOVA using GraphPad Prism 5. \* $P < 0.05$  was considered statistically significant, and extreme significance was set at \*\* $P < 0.01$ .

## 3. Results and discussion

### 3.1. Synthesis and characterization of MSN and MSN-NH<sub>2</sub>

Fig. 2A shows the Cryo-TEM images of MSN. As depicted, the as-prepared MSN were well-dispersed nanospheres with uniform particle sizes of about 80 nm, the apparent worm-like pores were averagely arranged throughout the entire particle. The N<sub>2</sub> adsorption-desorption isotherms (Fig. S1A) exhibited a characteristic type IV isotherm according to the International Union of Pure and Applied Chemistry (IUPAC) classification [25] demonstrating their mesoporous characteristic channels, large Brunauer-Emmett-Teller surface area (863.45 m<sup>2</sup>/g) and cumulative pore volume (0.68 cm<sup>3</sup>/g). Correspondingly, the Barrett-Joyner-Halenda (BJH) pore-size distribution of MSN exhibited a single peak and implied a narrow pore distribution with average diameters of 2.72 nm (Fig. S1B). The Cryo-TEM image of MSN-NH<sub>2</sub> were seen in Fig. 2B, the morphology and dispersivity of MSN-NH<sub>2</sub> were almost the

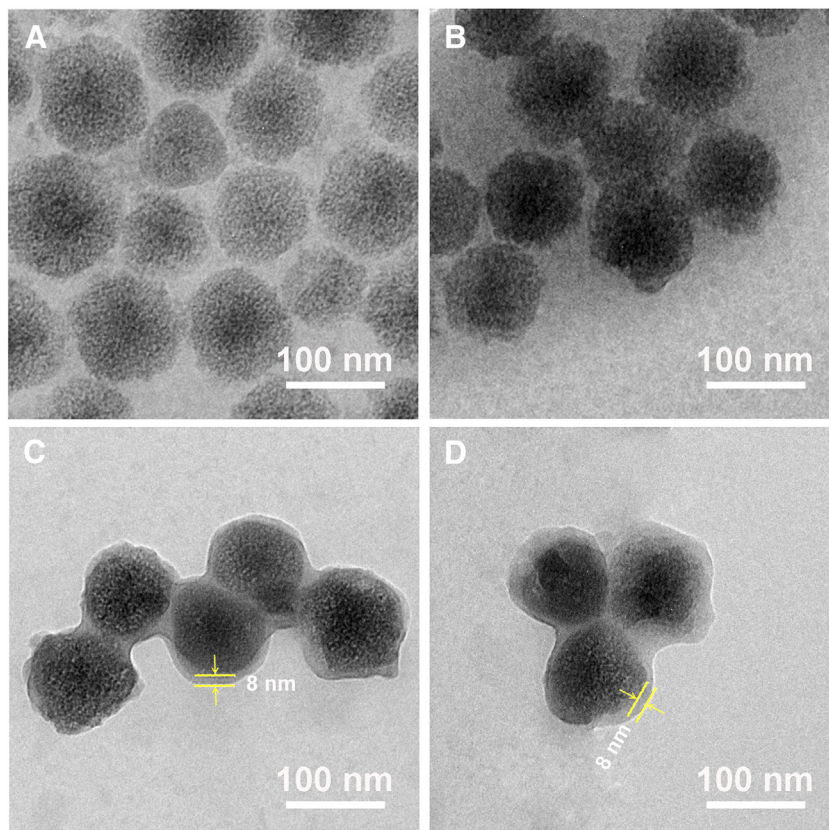


Fig. 2. Cryo-TEM images of MSN (A), MSN-NH<sub>2</sub> (B), M-SPC-L(E + D) (C) and M-HHG<sub>2</sub>C<sub>18</sub>-L(E + D) (D).

same as those MSN. The reduction of mesopores suggested that the amino groups had been grafted on MSN. MSN-NH<sub>2</sub> exhibited a similar type of N<sub>2</sub> adsorption–desorption isotherm with MSN, however, the introduction of amino groups caused a reduction in surface area and pore diameter (Fig. S1B and Table S1).

The presence of the aminopropyl functional groups can be further confirmed by the FTIR measurements. Compared with MSN, the FTIR spectra of as-synthesized MSN-NH<sub>2</sub> (Fig. S2B) presented a new band at 1558.48 cm<sup>-1</sup> ascribed to NH<sub>2</sub> bending [26], and the other new bands assigned to the stretching vibration of CH<sub>2</sub> appear at 2933.73 cm<sup>-1</sup> due to methyl group introduced during silylation [26,27]. This suggested that the amino groups were successfully grafted onto the surfaces of MSN. The surface coverage of amino groups could be estimated from fluorescamine measurements and up to 1.69 mmol/g was found on the MSN.

### 3.2. Preparation of M-HHG<sub>2</sub>C<sub>18</sub>-L(E + D) and M-SPC-L(E + D)

The non-sensitive lipid bilayer (SPC-L) was consisted of SPC and Chol. HHG<sub>2</sub>C<sub>18</sub> was anchored into the membrane of SPC-L to construct pH-sensitive lipid bilayer (HHG<sub>2</sub>C<sub>18</sub>-L). Both SPC-L and HHG<sub>2</sub>C<sub>18</sub>-L were electrostatically attached onto the surfaces of MSN-NH<sub>2</sub> to form

lipid bilayer supported MSN-NH<sub>2</sub>. The successful coating process was evidenced by a sharp change of zeta potential from 23 mV to -28/-38 mV, respectively. Cryo-TEM investigation of M-SPC-L(E + D) (Fig. 2C) and M-HHG<sub>2</sub>C<sub>18</sub>-L(E + D) (Fig. 2D) also provided direct visual evidence of the uniform coating of the surfaces with an intact SPC-L/HHG<sub>2</sub>C<sub>18</sub>-L of ~8 nm. Erlotinib and DOX were efficiently encapsulated into the lipid bilayer and MSN-NH<sub>2</sub>, respectively. The corresponding encapsulation efficiency of erlotinib and DOX were higher than 50% and 93%, respectively.

### 3.3. pH-sensitive charge conversional behavior

It has been demonstrated that the zwitterionic oligopeptide lipids contained in HHG<sub>2</sub>C<sub>18</sub>-L was pH-sensitive charge conversion to the surrounding pH [22]. Thus the pH-sensitive charge conversional feature of M-HHG<sub>2</sub>C<sub>18</sub>-L(E + D) was assessed by the zeta-potential analysis using M-SPC-L(E + D) as a control at several pH values ranging from 7.4 to 4.5. As shown in Fig. 3A, for M-SPC-L(E + D), no charge-conversional behavior was observed, and its zeta potential stayed negative. While zeta potential of M-HHG<sub>2</sub>C<sub>18</sub>-L(E + D) changed from -38 mV to 4.5 mV as pH value decreased from 7.4 to 6.5, and became more positive (22 mV) at pH 5.5 or 4.5, which was mainly

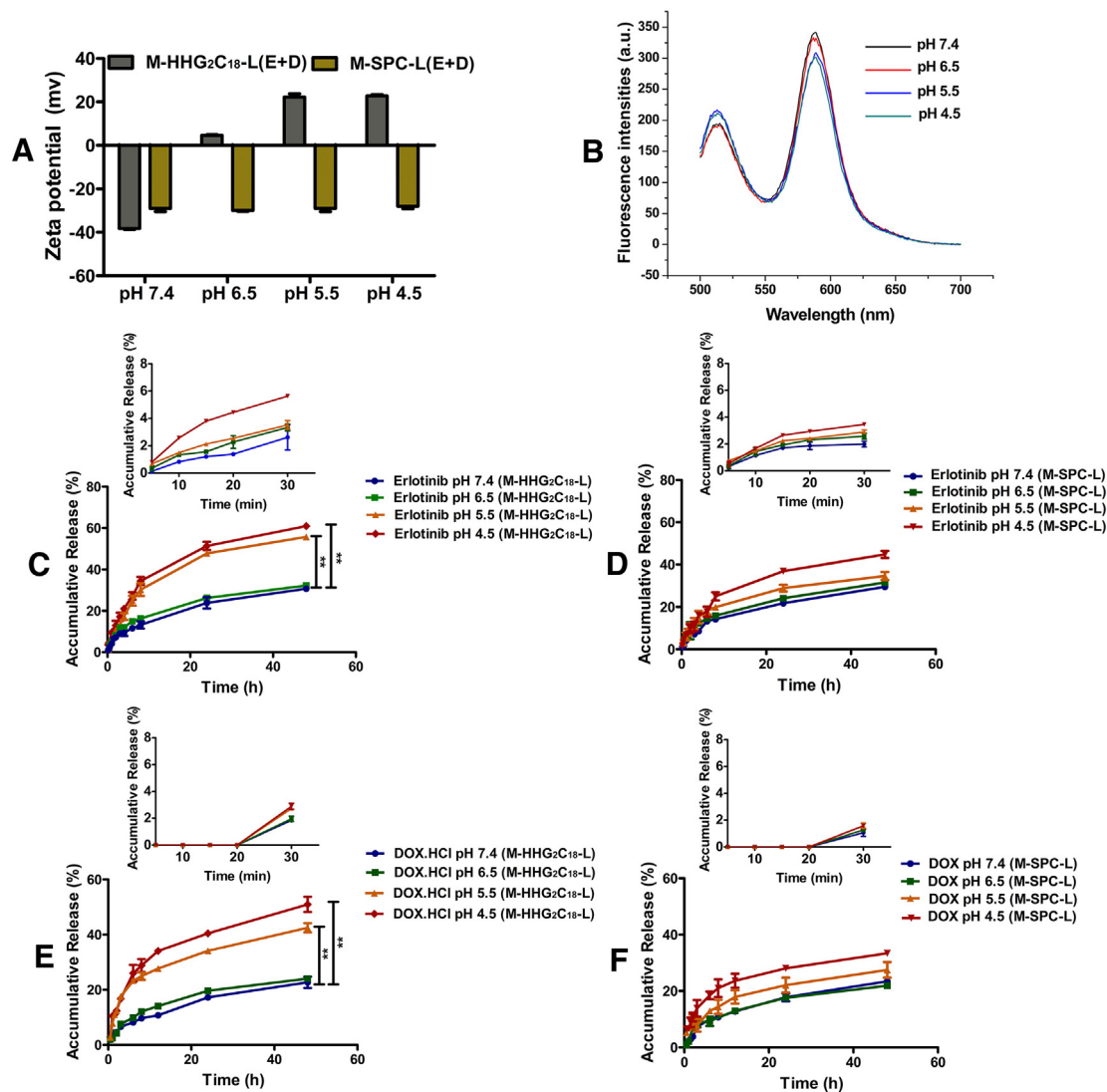


**Fig. 3.** Zeta potential of M-HHG<sub>2</sub>C<sub>18</sub>-L(E + D) and M-SPC-L(E + D) at different pH values (A). Fluorescence spectra of the FRET M-HHG<sub>2</sub>C<sub>18</sub>-L at the excitation wavelength of 485 nm at series of pH values (B). In vitro erlotinib (C–D) and DOX (E–F) release profiles from M-HHG<sub>2</sub>C<sub>18</sub>-L(E + D) or M-SPC-L(E + D) at different pH values. Data are shown as mean ± SD (n = 3). \*\*P < 0.01.

attributed to the protonation/deprotonation of carboxyl group of hexahydrobenzoic acid and the amino group of histidine included in HHG<sub>2</sub>C<sub>18</sub>-L [22]. Compared with non-charge conversional M-SPC-L(E + D), the zeta potential of M-HHG<sub>2</sub>C<sub>18</sub>-L(E + D) was more negative at pH 7.4 due to the introduction of more carboxyl groups of HHG<sub>2</sub>C<sub>18</sub>-L on the nanoparticle surface. Overall, these results demonstrated that M-HHG<sub>2</sub>C<sub>18</sub>-L(E + D) were capable of reversing the zeta potential according to the surrounding pH. In particular, it was also confirmed that charge conversion of M-HHG<sub>2</sub>C<sub>18</sub>-L(E + D) from negative to positive occurred at p*H*<sub>e</sub> and more positively charged at p*H*<sub>i</sub>.

To investigate whether the state between the supported HHG<sub>2</sub>C<sub>18</sub>-L and MSN-NH<sub>2</sub> was destabilized at acidic pH values, especially at pH 5.5 or 4.5 which was conducive to drug release. We designed fluorescence resonance energy transfer (FRET) M-HHG<sub>2</sub>C<sub>18</sub>-L composed of fluorescein isothiocyanate ester (FITC) modified MSN-NH<sub>2</sub> (MSN-NH<sub>2</sub>-FITC) and rhodamine B labeled HHG<sub>2</sub>C<sub>18</sub>-L and further tested the FRET phenomenon of FRET M-HHG<sub>2</sub>C<sub>18</sub>-L at different pH values (7.4, 6.5, 5.5, 4.5). As shown from Fig. 3B, at all pH values, an excitation at 485 nm, corresponding to the FITC excitation wavelength, produced apparent emission of the rhodamine B because of energy transfer from FITC donor to rhodamine B acceptor. Additionally, similar FRET signals were observed at pH 7.4 and pH 6.5, with FRET efficiency of 64.74% and 63.66%, respectively. However, FRET interaction between MSN-NH<sub>2</sub>-FITC and rhodamine B labeled HHG<sub>2</sub>C<sub>18</sub>-L was disrupted when the nanoparticles were located in pH 5.5 and pH 4.5 buffer, which were evidenced by the increased FITC signal together with the decreased rhodamine B signal or the decreased FRET efficiency of 58.81% and 58.78%, respectively. These results indicated that, at pH 5.5 or pH 4.5, the state between HHG<sub>2</sub>C<sub>18</sub>-L shell and MSN-NH<sub>2</sub> core was destabilized owing to Coulombic repulsion originated from positively charged HHG<sub>2</sub>C<sub>18</sub>-L and MSN-NH<sub>2</sub>. While the less positive HHG<sub>2</sub>C<sub>18</sub>-L could not cause Coulombic repulsion strong enough to impact the state between “core” and “shell” of M-HHG<sub>2</sub>C<sub>18</sub>-L at pH 6.5.

### 3.4. *In vitro* drug release

The dialysis method was used to study the release properties of M-HHG<sub>2</sub>C<sub>18</sub>-L(E + D) in PBS buffers with different pH values (7.4, 6.5, 5.5, 4.5) at 37 °C. For comparison, the release of erlotinib and DOX from non-sensitive M-SPC-L(E + D) were also monitored. Fig. 3C–F exhibits the *in-vitro* release profiles of M-HHG<sub>2</sub>C<sub>18</sub>-L(E + D) and M-SPC-L(E + D) for erlotinib and DOX. At all test pH of PBS buffers, both M-HHG<sub>2</sub>C<sub>18</sub>-L(E + D) and M-SPC-L(E + D) showed no release of DOX within 20 min. However, 2.6–5.6% of erlotinib released at pH 7.4–4.5 for M-HHG<sub>2</sub>C<sub>18</sub>-L(E + D), and 2.0–3.4% of erlotinib released at pH 7.4–4.5 for M-SPC-L(E + D). This demonstrated that erlotinib released faster than DOX. We supposed that since erlotinib was entrapped in the exterior lipid bilayer and DOX was loaded in the interior MSN-NH<sub>2</sub> core of nanocarrier, erlotinib would release faster than DOX. Besides, the strong adsorption capacity of MSN-NH<sub>2</sub> for DOX might also contribute to a slower release rate for DOX than erlotinib. Within 48 h, M-HHG<sub>2</sub>C<sub>18</sub>-L(E + D) and M-SPC-L(E + D) had similar and relatively slow drug release at pH 7.4 and pH 6.5. However, M-HHG<sub>2</sub>C<sub>18</sub>-L(E + D) showed higher release rate of erlotinib and DOX than that of M-SPC-L(E + D) at pH 5.5 and pH 4.5. M-HHG<sub>2</sub>C<sub>18</sub>-L(E + D) exhibited slightly increased drug release at pH 6.5 than that at pH 7.4, however, as pH decreased to 5.5 or 4.5, the drug release rates of M-HHG<sub>2</sub>C<sub>18</sub>-L(E + D) were obviously increased, 56% of erlotinib and 43% of DOX had been released at pH 5.5 after 48 h, which were higher than that at pH 7.4 and pH 6.5, additionally, 61% of erlotinib and 51% of DOX had been released at pH 4.5 after 48 h, which were higher than that at pH 5.5. It was explained that at pH 6.5, the positively charged lipid bilayer of M-HHG<sub>2</sub>C<sub>18</sub>-L(E + D) could not cause enough repulsion force with MSN-NH<sub>2</sub> to disrupt the interaction state between lipid bilayer and MSN-NH<sub>2</sub>, which led to a similar “core-shell” state of M-HHG<sub>2</sub>C<sub>18</sub>-L(E + D) at pH 6.5 and pH 7.4, thus the drug release profiles were little different between pH 6.5 and pH 7.4.

However, at pH 5.5 or 4.5, the state between HHG<sub>2</sub>C<sub>18</sub>-L and MSN-NH<sub>2</sub> was disrupted by strong electrostatic repulsion between HHG<sub>2</sub>C<sub>18</sub>-L and MSN-NH<sub>2</sub>, resulting in significant increase of drug release. For M-SPC-L(E + D), the difference in drug release between different pH values was not obvious. This mainly due to the fact that the “core-shell” state of M-SPC-L(E + D) under all test pH was similar and the drug release depended on self-diffusion release.

### 3.5. Cellular uptake and endocytosis pathway

To investigate whether the pH-sensitive charge conversional property of M-HHG<sub>2</sub>C<sub>18</sub>-L(E + D) facilitates cellular uptake at tumor extracellular pH, human non-small-cell lung cancer A549 cells were incubated with M-HHG<sub>2</sub>C<sub>18</sub>-L(E + D) and non-sensitive M-SPC-L(E + D) at pH 7.4 and pH 6.5 for 4 h, respectively. As shown in Fig. 4A, the cellular uptake of Si element at pH 6.5 was higher than that at pH 7.4 for M-HHG<sub>2</sub>C<sub>18</sub>-L(E + D), this may be due to the fact that M-HHG<sub>2</sub>C<sub>18</sub>-L(E + D) reversed to be positive at pH 6.5, leading to electrostatic absorption on cell membrane, thus facilitating cellular uptake [28]. However, for M-SPC-L(E + D) group, the cellular uptake of Si element showed no obvious difference between pH 7.4 and pH 6.5, it was explained that M-SPC-L(E + D) stayed negative at pH 6.5, lacking charge-activated cellular uptake. These results indicated that the pH-sensitive charge conversional property significantly facilitated cellular uptake of nanocarrier. Additionally, the cellular uptake of erlotinib (Fig. 4B) and DOX (Fig. 4C) at pH 6.5 were significantly higher than that at pH 7.4 for M-HHG<sub>2</sub>C<sub>18</sub>-L(E + D). Whereas, for M-SPC-L(E + D), the cellular uptake of erlotinib and DOX showed no obvious change between pH 7.4 and pH 6.5, this may attribute to the different cellular uptake between M-HHG<sub>2</sub>C<sub>18</sub>-L and M-SPC-L at pH 7.4 and pH 6.5, the cellular uptake of loaded drugs was proportional to the cellular uptake of the corresponding nanocarrier.

To qualitatively demonstrate that M-HHG<sub>2</sub>C<sub>18</sub>-L(E + D) can be more efficiently internalized by cancer cells at extracellular pH and further delivery to cell nuclei. M-HHG<sub>2</sub>C<sub>18</sub>-L(E + D) were co-incubated with A549 cells for 1 h, 4 h, 8 h and 12 h at pH 7.4 and pH 6.5 with corresponding DOX concentration of 2 µg/mL and observed by a confocal laser scanning microscope (CLSM, ZEISS LSM700, Germany). As shown in Fig. 4F, the cell nuclei were stained blue with DAPI and the red fluorescence was from DOX. After 1 h, red fluorescence was obvious distribution in the cytoplasm, suggesting that M-HHG<sub>2</sub>C<sub>18</sub>-L(E + D) were rapidly internalized by cancer cells after incubation for 1 h. As the incubation period increased, red fluorescence became stronger and distributed widely in the cytoplasm, indicating that the cellular uptake of M-HHG<sub>2</sub>C<sub>18</sub>-L(E + D) was time-independent. The DOX-related fluorescence showed a significant difference between pH 7.4 and 6.5 for M-HG<sub>2</sub>C<sub>18</sub>-L(E + D), stronger red fluorescence was observed in cells at pH 6.5, this result was due to the higher cellular uptake of M-HHG<sub>2</sub>C<sub>18</sub>-L(E + D) at pH 6.5 than that at pH 7.4. The red fluorescence of DOX was obvious in the cell nuclei after 8 h of incubation, and the fluorescence became stronger at a longer incubation time of 12 h. The cellular uptake of non-charge conversional M-SPC-L(E + D) was also observed by CLSM. As seen from Fig. 4F, for M-SPC-L(E + D) group, very weak DOX fluorescence was observed in cell nuclei even for 12 h of incubation, besides, DOX fluorescence in cells showed no difference at pH 7.4 and pH 6.5. These results indicated that M-HHG<sub>2</sub>C<sub>18</sub>-L(E + D) were capable to enhance the cellular uptake at pH 6.5, resulting from the high electrostatic interaction between positively charged M-HHG<sub>2</sub>C<sub>18</sub>-L(E + D) and cell membrane. After cellular uptake, the positively charged HHG<sub>2</sub>C<sub>18</sub>-L caused electrostatic repulsion with the interior MSN-NH<sub>2</sub> in the acid endosomal/lysosomal pH, leading to increase DOX release and give a strong ability of DOX to enter into the cell nuclei after endo-lysosomal escapes as result of the proton sponge effect of histidines in HHG<sub>2</sub>C<sub>18</sub>-L [22].

In an effort to identify the uptake mechanisms involved in the cellular entry of M-HHG<sub>2</sub>C<sub>18</sub>-L and non-sensitive nanocarrier (M-SPC-

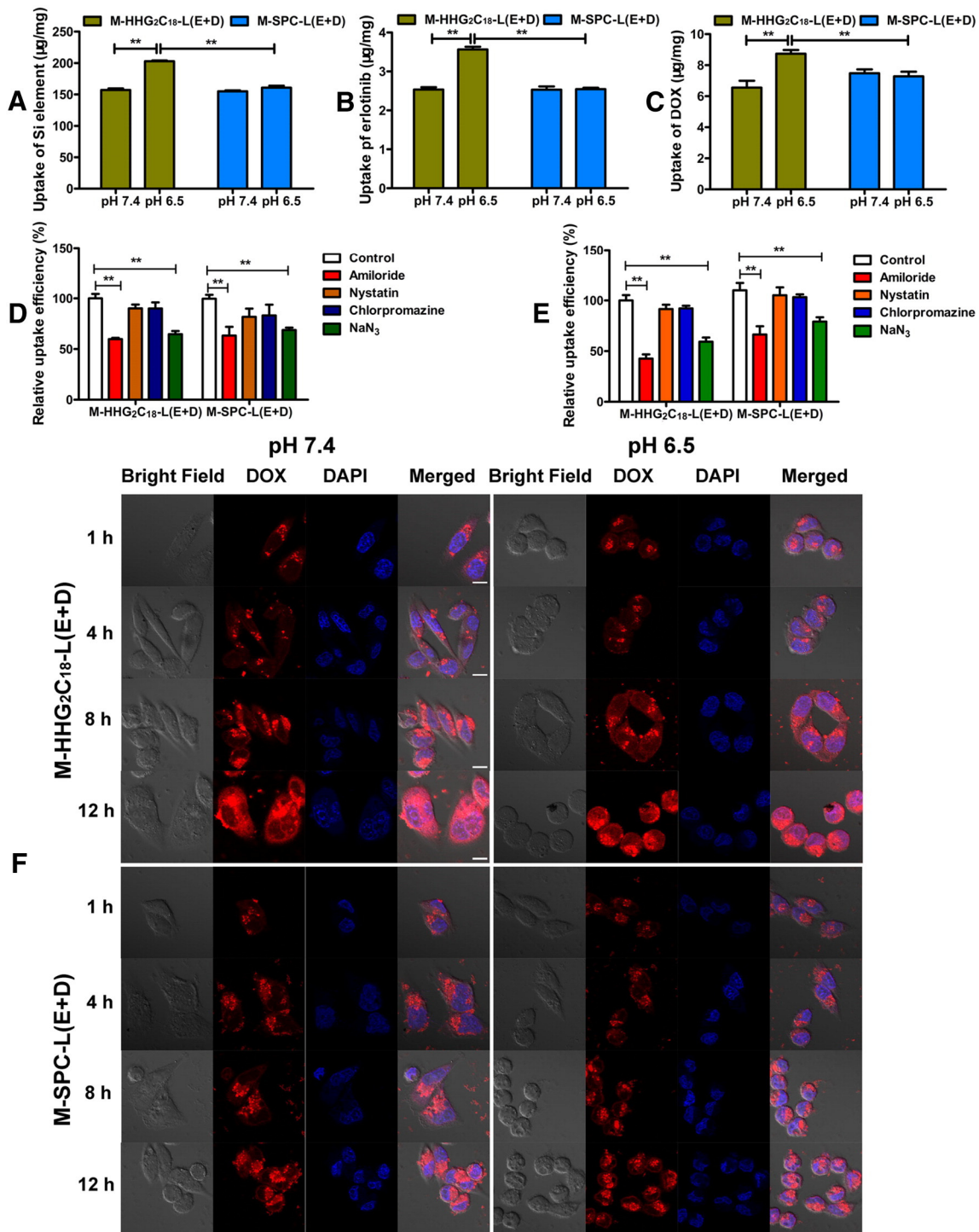


**Fig. 4.** Cellular uptake of Si element (A), erlotinib (B) and DOX (C) at different pH values in A549 cells after 4 h of incubation with M-HHG<sub>2</sub>C<sub>18</sub>-L(E + D) or M-SPC-L(E + D). \*P < 0.05. Relative uptake efficiency of erlotinib (D) and DOX (E) on A549 cells after 4 h of incubation with M-HHG<sub>2</sub>C<sub>18</sub>-L(E + D) or M-SPC-L(E + D) in the presence of various endocytosis inhibitors. NaN<sub>3</sub>, chlorpromazine, amiloride, and nystatin are the inhibitors for the energy-mediated endocytosis, clathrin-mediated endocytosis, macropinocytosis and caveolin-mediated endocytosis, respectively. \*\*P < 0.01, \*P < 0.05. Fluorescence visualization of DOX intracellular accumulation (F): A549 cells were treated with M-HHG<sub>2</sub>C<sub>18</sub>-L(E + D) or M-SPC-L(E + D) at pH 6.5 and 7.4 for 1 h, 4 h, 8 h, and 12 h (DOX concentration was 2 µg/mL). DAPI (blue); DOX (red). Scale bar: 10 µm.

L), several blockers of specific cellular internalization pathways were employed, respectively. As shown in Fig. 4D–E, both of the cellular uptake of M-HHG<sub>2</sub>C<sub>18</sub>-L(E + D) and M-SPC-L(E + D) decreased remarkably in the presence of amiloride, an inhibitor of macropinocytosis [29–31], and similar phenomena was observed in the presence of NaN<sub>3</sub>, an inhibitor of energy-mediated endocytosis [32–34]. Whereas, no

significant inhibition were found in the cases of nystatin and chlorpromazine, an inhibitor of caveolin-mediated endocytosis [35, 36] and clathrin-mediated endocytosis [37–39], respectively. Collectively, these results suggested that M-HHG<sub>2</sub>C<sub>18</sub>-L and M-SPC-L predominantly were taken up via energy-mediated macropinocytosis. It was noteworthy that internalization through macropinocytosis

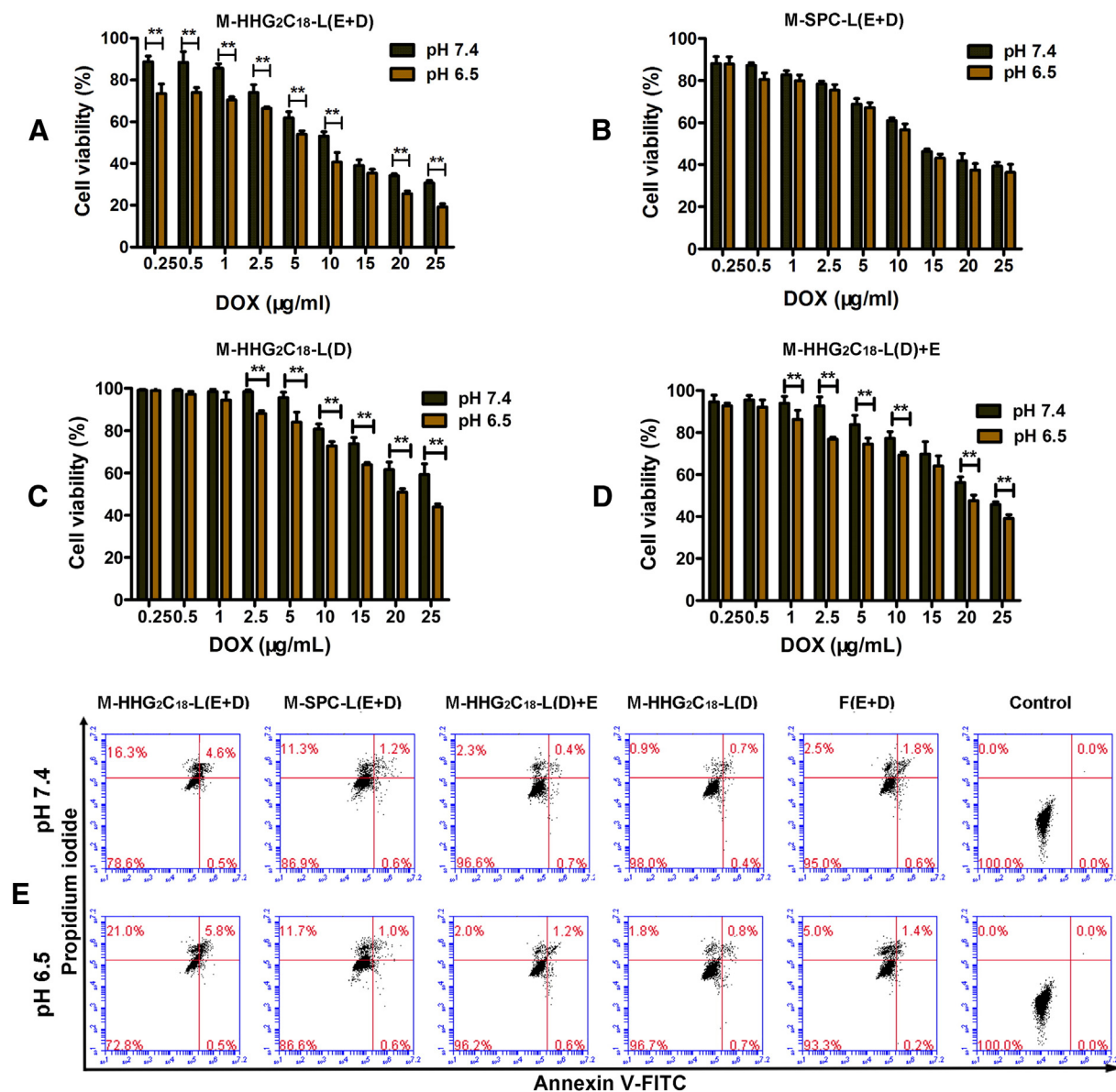


**Fig. 5.** In vitro cytotoxicity of M-HHG<sub>2</sub>C<sub>18</sub>-L(E + D) (A), M-SPC-L(E + D) (B), M-HHG<sub>2</sub>C<sub>18</sub>-L(D) (C) and M-HHG<sub>2</sub>C<sub>18</sub>-L(D) + E (D) on A549 cells at pH 7.4 and pH 6.5 for 24 h. \*\*P < 0.01. Cell apoptosis induced by different drug formulations at pH 7.4 and pH 6.5 for 12 h by using Annexin V-FITC/PI staining (E).

was indeed effective, since macropinosomes have a considerable porous membrane structure for enhanced leakage of inclusions into cytoplasm [40].

### 3.6. In vitro cytotoxicity and cell apoptosis

To investigate whether the pH-sensitive charge reversal property makes M-HHG<sub>2</sub>C<sub>18</sub>-L(E + D) more synergistic effect in cancer cell killing, the in vitro cytotoxicity of M-HHG<sub>2</sub>C<sub>18</sub>-L(E + D) against cancer cells was evaluated at pH 7.4 and pH 6.5 by MTT assay and compared

with non-sensitive M-SPC-L(E + D). As shown in Fig. 5A–B, both erlotinib/DOX-loaded formulations showed dose-dependent cytotoxic effects. In addition, M-HHG<sub>2</sub>C<sub>18</sub>-L(E + D) showed significantly enhanced toxicity at pH 6.5 relative to that at pH 7.4 after incubation for 24 h, and higher cytotoxic effect than M-SPC-L(E + D) at pH 6.5 at all the DOX concentrations studied. The IC<sub>50</sub> of M-HHG<sub>2</sub>C<sub>18</sub>-L(E + D) was about 5.81 µg/mL at pH 6.5, about 1.94-fold improved relative to that at pH 7.4. However, the cytotoxicity of M-SPC-L(E + D) had no remarkable improvement from pH 7.4 to pH 6.5 (Fig. 5B and Table S2). These results may be due to the enhanced

**Table 1**  
Pharmacokinetic parameters of erlotinib after intravenous injection of different erlotinib/DOX formulations at DOX dose of 5 mg/kg and erlotinib dose of 1.92 mg/kg in rats.

Samples	C <sub>max</sub> (µg/mL)	AUC (µg/mL·h)	T <sub>1/2</sub> (h)	MRT (h)	Clearance mg·h (µg/mL)
M-HHG <sub>2</sub> C <sub>18</sub> -L(E + D)	0.34 ± 0.04	0.54 ± 0.10*	2.79 ± 0.70*	4.17 ± 1.35*	3.07 ± 0.73*
M-SPC-L(E + D)	0.30 ± 0.09	0.50 ± 0.10*	2.54 ± 0.85*	3.28 ± 1.21*	3.40 ± 0.34*
F(E + D)	0.23 ± 0.05	0.29 ± 0.05	1.41 ± 0.13	1.75 ± 0.16	6.27 ± 0.98

\* P < 0.01 vs F(E + D).

**Table 2**

Pharmacokinetic parameters of DOX after intravenous injection of different erlotinib/DOX formulations at DOX dose of 5 mg/kg and erlotinib dose of 1.92 mg/kg in rats.

Samples	C <sub>max</sub> (μg/mL)	AUC (μg/mL·h)	T <sub>1/2</sub> (h)	MRT (h)	Clearance mg <sup>*</sup> h (μg/mL)
M-HHG <sub>2</sub> C <sub>18</sub> -L(E + D)	2.29 ± 0.48**	6.26 ± 0.47**	3.19 ± 0.62**	4.64 ± 0.40*	0.66 ± 0.04**
M-SPC-L(E + D)	1.58 ± 0.54	5.16 ± 0.67**	2.88 ± 1.09*	4.70 ± 0.99*	0.80 ± 0.05
F(E + D)	0.83 ± 0.91	2.88 ± 0.47	1.81 ± 0.24	3.27 ± 0.41	1.62 ± 0.22

\* P &lt; 0.05 vs F(E + D).

\*\* P &lt; 0.01 vs F(E + D).

cellular uptake of pH-sensitive charge conversion of M-HHG<sub>2</sub>C<sub>18</sub>-L(E + D) at pH<sub>e</sub> and accelerated drug release in intracellular environment, which significantly improved the synergistic effect of erlotinib/DOX combination.

The cytotoxicity of M-HHG<sub>2</sub>C<sub>18</sub>-L(D)) (Fig. 5C) and M-HHG<sub>2</sub>C<sub>18</sub>-L(D) + E (Fig. 5D) was also evaluated. We observed that both M-HHG<sub>2</sub>C<sub>18</sub>-L(D) + E and M-HHG<sub>2</sub>C<sub>18</sub>-L(D) exhibited low cytotoxicity although both were more effective cell killing at pH 6.5 than pH 7.4. M-HHG<sub>2</sub>C<sub>18</sub>-L(D) + E only presented a negligible increase of cytotoxicity than M-HHG<sub>2</sub>C<sub>18</sub>-L(D) under the same conditions. The results suggested that only the time-staggered drug release from a single nanocarrier, but not simultaneous coadministration remarkably improved the synergistic cancer cell killing effect of erlotinib/DOX combination. The bare M-HHG<sub>2</sub>C<sub>18</sub>-L and M-SPC-L had no cytotoxicity under the same conditions up to a total MSN-NH<sub>2</sub> concentration of 1 mg/mL (Fig. S3). The cytotoxicity of F(E + D) was also shown in Fig. S3 and Table S2.

Apoptosis-inducing effect of different erlotinib/DOX formulations were evidenced by an Annexin-V-FITC/PI method which was conducted by flow cytometry. The quantities of the early apoptotic cells, the late

apoptotic and necrotic cells, and the living cells were determined by the percentage of Annexin V<sup>+</sup>/PI<sup>-</sup>, Annexin V<sup>+</sup>/PI<sup>+</sup> and Annexin V<sup>-</sup>/PI<sup>-</sup>. Using the knowledge of synergistic combination therapies that exposure to the EGFR inhibitor erlotinib renders the cells susceptible to apoptosis in response to subsequent exposure to the DNA damaging agent doxorubicin [15], M-HHG<sub>2</sub>C<sub>18</sub>-L(E + D) had been confirmed to have the greatest effect in all the groups on inducing cancer cell apoptosis (Fig. 5E) after cell incubation for 12 h at both pH 7.4 and pH 6.5. The total apoptotic ratio of M-HHG<sub>2</sub>C<sub>18</sub>-L(E + D) increased from 5.1% at pH 7.4 to 6.3% at pH 6.5 after cell incubation for 12 h. Similarly, M-HHG<sub>2</sub>C<sub>18</sub>-L(D) + E and M-HHG<sub>2</sub>C<sub>18</sub>-L(D) slightly improve cell apoptosis at pH 6.5 relative to pH 7.4. On the contrary, M-SPC-L(E + D) exhibited neglectable change in cell apoptosis. It could be explained that M-HHG<sub>2</sub>C<sub>18</sub>-L(E + D) could reverse their surface charge from negative to positive at pH<sub>e</sub> for improved endocytosis and had capabilities of pH<sub>i</sub>-triggered efficient intracellular drug release, early and time-staggered suppression of EGFR signaling as well as effective nucleus targeting, thereby leading to the enhancement of antiproliferation and cell apoptosis.

According to these results above, it was indicated that M-HHG<sub>2</sub>C<sub>18</sub>-L as vector delivering synergistic erlotinib/DOX combination in same cells

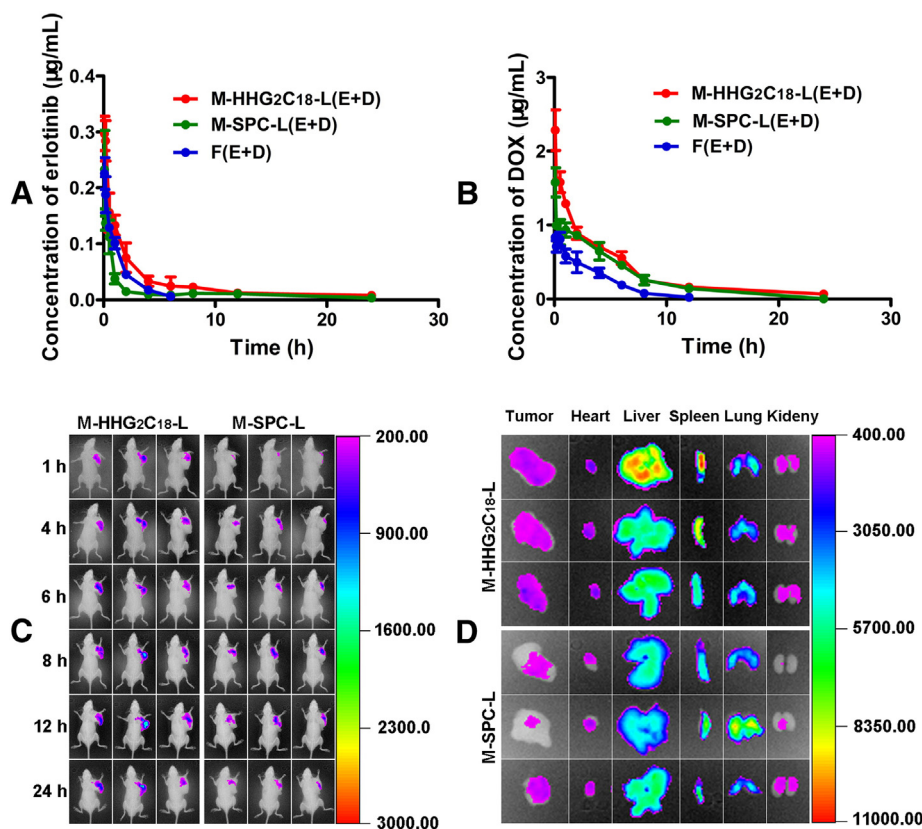


**Fig. 6.** Plasma concentration–time curve of erlotinib (A) and DOX (B) in the rats after intravenous injection of various erlotinib/DOX combination formulations at DOX dose of 5 mg/kg and erlotinib dose of 1.92 mg/kg. In vivo imaging of biodistribution of DIR contained M-HHG<sub>2</sub>C<sub>18</sub>-L or M-SPC-L (n = 3) at different time points after intravenous injection into the LLC tumor-bearing mice (C). Accumulation of DIR-labeled M-HHG<sub>2</sub>C<sub>18</sub>-L or M-SPC-L in the tumor and different organs detected using the ex vivo imaging at 24 h post-injection (D).

in vitro was successful because the highest apoptosis rate obtained as cells treated by M-HHG<sub>2</sub>C<sub>18</sub>-L(E + D).

### 3.7. Pharmacokinetics and biodistribution

The pharmacokinetic behaviors of erlotinib and DOX were investigated after intravenous administration of the three formulations (M-HHG<sub>2</sub>C<sub>18</sub>-L(E + D), M-SPC-L(E + D) and F(E + D)). The corresponding pharmacokinetic parameters were reported in Table 1 / Table 2.

Both the maximum plasma concentration ( $C_{max}$ ) and the area under the plasma concentration–time curve (AUC) of F(E + D) were conspicuously lower than that of erlotinib/DOX-loaded nanoparticles, which manifested that the nanoparticles as encapsulating matrix of anticancer drugs package played a remarkable role in reducing the blood clearance and prolonging the circulating time. M-HHG<sub>2</sub>C<sub>18</sub>-L(E + D) and M-SPC-L(E + D) presented similar pharmacokinetic profiles (Fig. 6A–B). Comparison with free drug combination, M-HHG<sub>2</sub>C<sub>18</sub>-L highly increased AUC to 1.9/2.2-fold, the plasma elimination half-life ( $T_{1/2}$ ) to 2.0/1.8-fold and mean residence time (MRT) to 2.4/1.4-fold for erlotinib/DOX, demonstrating that M-HHG<sub>2</sub>C<sub>18</sub>-L enhanced the bioavailability and blood persistence of erlotinib and DOX, and potentially improved the tumor target-ability and therapeutic index in vivo.

The biodistribution of M-HHG<sub>2</sub>C<sub>18</sub>-L and M-SPC-L after intravenous injection into the Lewis lung carcinoma (LLC) tumor-bearing mice were monitored using the in vivo imaging technique. M-HHG<sub>2</sub>C<sub>18</sub>-L and M-SPC-L were labeled with DIR. As shown in Fig. 6C, M-HHG<sub>2</sub>C<sub>18</sub>-L and M-SPC-L possessed a similar distribution profile in vivo, which was consistent with pharmacokinetic profiles. Both M-HHG<sub>2</sub>C<sub>18</sub>-L and M-SPC-L demonstrated good tumor accumulation as a result of the EPR effect. The DIR fluorescence signals were observed in tumor site at 1 h after administration, the strongest fluorescence intensities were observed at 8 h and declined gradually as time increased. Interestingly, the duration of fluorescence in tumors reached 24 h and the fluorescence intensity was still strong on the tumor position. At 24 h post-injection, the mice were sacrificed by cervical dislocation, and the tumor as well as major organs, including heart, liver, spleen, lung and kidney were excised for ex vivo imaging (Fig. 6D). Strong DIR fluorescence was observed at tumor. However fluorescence signal also distributed in liver and kidney. Such a behavior is expected for intravenously injected nanomaterials with passive targeting and indicated that the in vivo fate of DIR-containing M-HHG<sub>2</sub>C<sub>18</sub>-L and M-SPC-L involved hepatic clearance and renal excretion [41]. The tumors were also conducted with the frozen tissue section and observed using CLSM. The red signals from DIR in tumor tissue section (Fig. S4) further confirmed the tumor-targeting ability of M-HHG<sub>2</sub>C<sub>18</sub>-L and M-SPC-L.

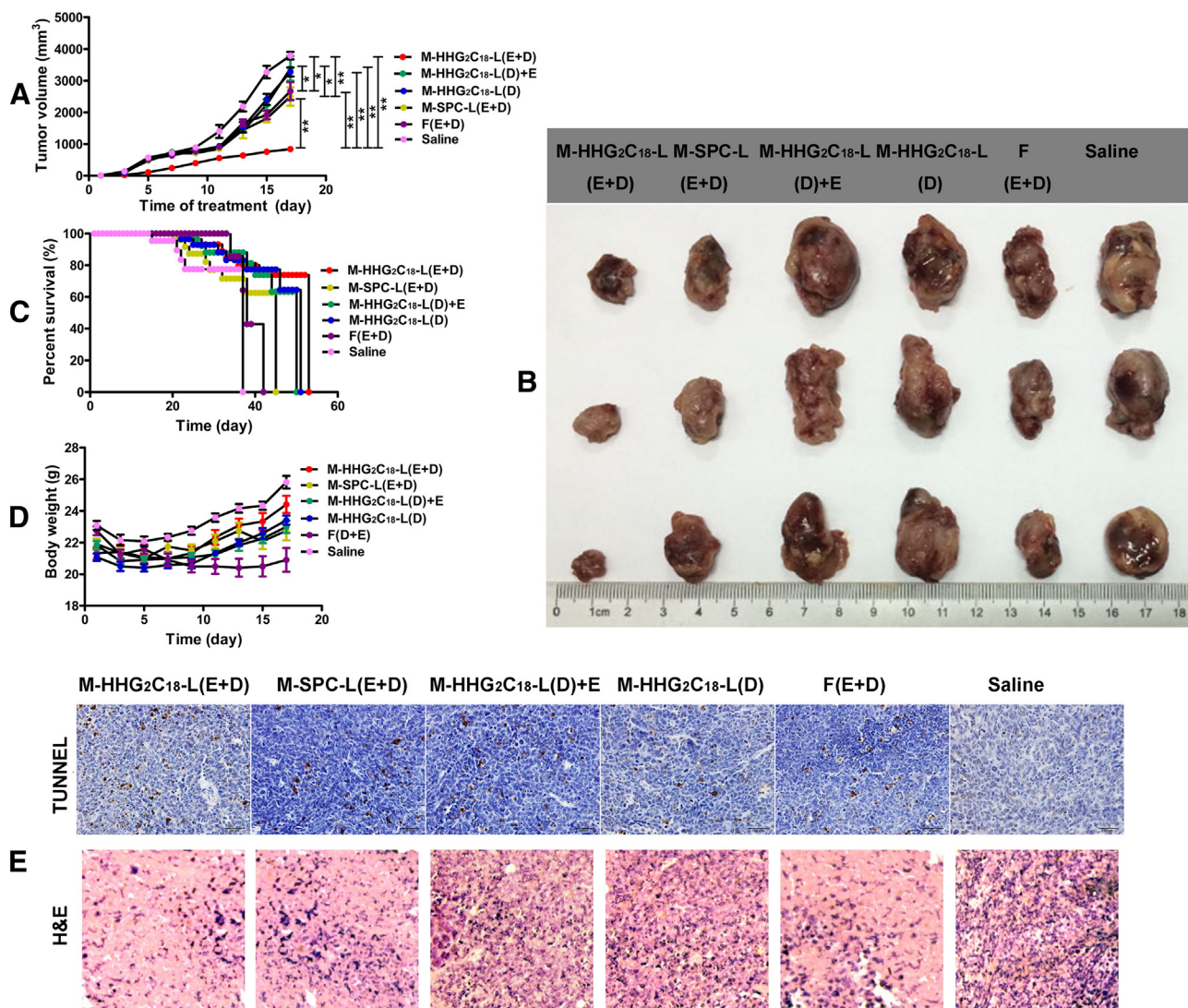


Fig. 7. The tumor growth curves (A), images of excised LLC tumors (B), survival periods (C), body weight changes (D) and histological changes (E) of tumor sections of the LLC tumor-bearing mice receiving intravenous injection of different formulations at DOX dose of 2 mg/kg and erlotinib dose of 0.77 mg/kg. \*\* $P < 0.01$ .

### 3.8. Antitumor efficacy in vivo

In order to further evaluate the anticancer potential of our pH-sensitive charge conversion co-delivery system, the effects of M-HHG<sub>2</sub>C<sub>18</sub>-L(E + D) compared to other drug formulations on tumor growth inhibition in LLC tumor-bearing mice were investigated. As shown in Fig. 7A, the tumor volume of mice administered saline as a control rapidly increased over 17 days, while M-SPC-L(E + D) and F(E + D) moderately inhibited tumor growth and M-HHG<sub>2</sub>C<sub>18</sub>-L(E + D) displayed the most dramatic tumor inhibition effect. In addition, we also evaluated the in vivo tumor inhibition efficiency of M-HHG<sub>2</sub>C<sub>18</sub>-L(D) + E and M-HHG<sub>2</sub>C<sub>18</sub>-L(D) and no tumor inhibitory effects were found when compared with saline group. This result corresponded with the aforementioned data revealing in cytotoxicity and cell apoptosis. The excised tumors (Fig. 7B) also confirmed that M-HHG<sub>2</sub>C<sub>18</sub>-L(E + D) were more effective in reducing the tumor volume compared with M-SPC-L(E + D), F(E + D), M-HHG<sub>2</sub>C<sub>18</sub>-L(D) + E and M-HHG<sub>2</sub>C<sub>18</sub>-L(D). Additionally, M-HHG<sub>2</sub>C<sub>18</sub>-L(E + D) possessed the most distinguished effect on extending the survival period of the tumor bearing mice (Fig. 7C) with mean survival of 53 days.

We processed representative tumors harvested from various groups on day 17 after the first injection for histological analyses. H&E staining indicated that the M-HHG<sub>2</sub>C<sub>18</sub>-L(E + D) treated group rendered a lower cell density in the tumor tissue as compared with other four treated groups (Fig. 7E), validating that proliferation had been halted effectively in the M-HHG<sub>2</sub>C<sub>18</sub>-L(E + D) treated group. We also analyzed apoptosis in tumor tissue by the TUNEL method. TUNEL analysis (Fig. 7E) revealed that M-HHG<sub>2</sub>C<sub>18</sub>-L(E + D) induced much more significant cell apoptosis in tumors compared with M-SPC-L(E + D), M-HHG<sub>2</sub>C<sub>18</sub>-L(D) + E and M-HHG<sub>2</sub>C<sub>18</sub>-L(D), which was consistent with the H&E analysis. Taken together, these results demonstrated that M-HHG<sub>2</sub>C<sub>18</sub>-L(E + D) significantly inhibited LLC tumor growth in C57/BL6 mice model through suppression of cell proliferation and induction of apoptosis. Enhanced efficacy of M-HHG<sub>2</sub>C<sub>18</sub>-L(E + D) may be explained this way: (1) charge conversion from negative to positive increased cellular uptake in extracellular environment; (2) accelerated intracellular drug release owing to the Coulombic repulsion between HHG<sub>2</sub>C<sub>18</sub>-L and MSN-NH<sub>2</sub> in intracellular environment; (3) sequential staggered release of erlotinib and DOX improved synergistic effects of combination chemotherapy.

In respect to safety evaluation, the body weight variations in the treated mice were also monitored during the experimental period. As shown in Fig. 7D, no obvious body weight changes were observed in these mice except the F(E + D) group during the experimental period. About 15% body weight loss was detected in the F(E + D) treated group at the end of the experimental period indicating the severe toxicity of free DOX. These results suggested that there was no acute or severe toxicity related to nanocarrier-based treatment at the test dose. In addition, no obvious damage was observed to these major organs including heart, liver, spleen, lung and kidney (Fig. S5).

### 4. Conclusions

1. In summary, we successfully developed a pH-sensitive charge conversion M-HHG<sub>2</sub>C<sub>18</sub>-L to co-delivery synergistic erlotinib/DOX combination for lung cancer therapy. This charge conversion property enhanced the cellular uptake of M-HHG<sub>2</sub>C<sub>18</sub>-L(E + D) at tumor extracellular pH, and further led to remarkably enhanced drug release at tumor intracellular pH. M-HHG<sub>2</sub>C<sub>18</sub>-L(E + D) were capable of producing a sequential staggered drug release to maximize synergistic anticancer effect by sequence entrapment of erlotinib and DOX in the nanoparticles. Compared to other treatment groups, M-HHG<sub>2</sub>C<sub>18</sub>-L(E + D) showed great synergistic effects of combination chemotherapy against A549 cell line, potently suppressed tumor growth in established C57/BL6 Lewis lung carcinoma tumor xenograft models and significantly prolonged the survival period. The histological analysis revealed that M-HHG<sub>2</sub>C<sub>18</sub>-L(E + D) did not show

any damage to major organs under the experimental conditions. Therefore, these results revealed that M-HHG<sub>2</sub>C<sub>18</sub>-L(E + D) combined pH-sensitive charge conversion property with sequential staggered drug release feature were highly effective and potential as co-delivery system for cancer chemotherapy.

### Acknowledgments

This work was supported by the National Natural Science Foundation of China (81273468, 81473153, 81503006), the Natural Science Foundation of Jiangsu Province of China (BK20140672, BK20150698), the Hunan Provincial Innovation Foundation For Postgraduate (CX2013B043), 111 Project from the Ministry of Education of China and the State Administration of Foreign Expert Affairs of China (no. 111-2-07) and the Fundamental Research Funds for the Central Universities (1050010009).

### Appendix A. Supplementary data

Supplementary data to this article can be found online at <http://dx.doi.org/10.1016/j.jconrel.2016.03.001>.

### References

- [1] L.A. Torre, F. Bray, R.L. Siegel, J. Ferlay, J. Lortet-Tieulent, A. Jemal, Global cancer statistics, 2012, *CA Cancer J. Clin.* 65 (2015) 87–108.
- [2] C. Fitzmaurice, D. Dicker, A. Pain, H. Hamavid, M. Moradi-Lakeh, M.F. MacIntyre, et al., The global burden of cancer 2013, *JAMA Oncol.* 1 (2015) 505–527.
- [3] F. Danhier, O. Feron, V. Preat, To exploit the tumor microenvironment: passive and active tumor targeting of nanocarriers for anti-cancer drug delivery, *J. Control. Release* 148 (2010) 135–146.
- [4] Y. Chen, H. Chen, J. Shi, Inorganic nanoparticle-based drug codelivery nanosystems to overcome the multidrug resistance of cancer cells, *Mol. Pharm.* 11 (2014) 2495–2510.
- [5] D. Peer, J.M. Karp, S. Hong, O.C. Farokhzad, R. Margalit, R. Langer, Nanocarriers as an emerging platform for cancer therapy, *Nat. Nanotechnol.* 2 (2007) 751–760.
- [6] A.S. Lichter, T.S. Lawrence, Medical progress—recent advances in radiation oncology, *N. Engl. J. Med.* 332 (1995) 371–379.
- [7] C.E. Ashley, E.C. Carnes, G.K. Phillips, D. Padilla, P.N. Durfee, P.A. Brown, T.N. Hanna, J.W. Liu, B. Phillips, M.B. Carter, N.J. Carroll, X.M. Jiang, D.R. Dunphy, C.L. Willman, D.N. Petsev, D.G. Evans, A.N. Parikh, B. Chackerian, W. Wharton, D.S. Peabody, C.J. Brinker, The targeted delivery of multicomponent cargos to cancer cells by nanoporous particle-supported lipid bilayer, *Nat. Mater.* 10 (2011) 389–397.
- [8] L.Q. Cai, G.F. Xu, C.Y. Shi, D.D. Guo, X. Wang, J.T. Luo, Telodendrimer nanocarrier for co-delivery of paclitaxel and cisplatin: a synergistic combination nanotherapy for ovarian cancer treatment, *Biomaterials* 37 (2015) 456–468.
- [9] H. Meng, M. Wang, H. Liu, X. Liu, A. Situ, B. Wu, Z. Ji, C.H. Chang, A.E. Nel, Use of a lipid-coated mesoporous silica nanoparticle platform for synergistic gemcitabine and paclitaxel delivery to human pancreatic cancer in mice, *ACS Nano* 9 (2015) 3540–3557.
- [10] I. Noh, H.-O. Kim, J. Choi, D.K. Lee, Y.-M. Huh, S. Haam, Co-delivery of paclitaxel and gemcitabine via CD44-targeting nanocarriers as a prodrug with synergistic antitumor activity against human biliary cancer, *Biomaterials* 53 (2015) 763–774.
- [11] H. Wang, P. Agarwal, S.T. Zhao, R.X. Xu, J.H. Yu, X.B. Lu, X.M. He, Hyaluronic acid-decorated dual responsive nanoparticles of pluronic F127, PLGA, and chitosan for targeted co-delivery of doxorubicin and irinotecan to eliminate cancer stem-like cells, *Biomaterials* 72 (2015) 74–89.
- [12] W.W. Wang, H.J. Song, J. Zhang, P. Li, C. Li, C. Wang, D.L. Kong, Q. Zhao, An injectable, thermosensitive and multicompartement hydrogel for simultaneous encapsulation and independent release of a drug cocktail as an effective combination therapy platform, *J. Control. Release* 203 (2015) 57–66.
- [13] P. Zhang, J. Li, M. Ghazwani, W.C. Zhao, Y.X. Huang, X.L. Zhang, R. Venkataramanan, S. Li, Effective co-delivery of doxorubicin and dasatinib using a PEG-Fmoc nanocarrier for combination cancer chemotherapy, *Biomaterials* 67 (2015) 104–114.
- [14] A.G. Assanhou, W.Y. Li, L. Zhang, L.J. Xue, L.Y. Kong, H.B. Sun, R. Mo, C. Zhang, Reversal of multidrug resistance by co-delivery of paclitaxel and lonidamine using a TPGS and hyaluronic acid dual-functionalized liposome for cancer treatment, *Biomaterials* 73 (2015) 284–295.
- [15] M.J. Lee, A.S. Ye, A.K. Gardino, A.M. Heijink, P.K. Sorger, G. MacBeath, M.B. Yaffe, Sequential application of anticancer drugs enhances cell death by rewiring apoptotic signaling networks, *Cell* 149 (2012) 780–794.
- [16] A.J. Primeau, A. Rendon, D. Hedley, L. Lilge, I.F. Tannock, The distribution of the anticancer drug doxorubicin in relation to blood vessels in solid tumors, *Clin. Cancer Res.* 11 (2005) 8782–8788.
- [17] K. Huber, A. Feuchtinger, D.M. Borgmann, Z. Li, M. Aichler, S.M. Hauck, H. Zitzelsberger, M. Schwaiger, U. Keller, A. Walch, Novel approach of MALDI drug imaging, immunohistochemistry, and digital image analysis for drug distribution studies in tissues, *Anal. Chem.* 86 (2014) 10568–10575.

- [18] S.W. Morton, M.J. Lee, Z.J. Deng, E.C. Dreaden, E. Siouve, K.E. Shopsowitz, N.J. Shah, M.B. Yaffe, P.T. Hammond, A nanoparticle-based combination chemotherapy delivery system for enhanced tumor killing by dynamic rewiring of signaling pathways, *Sci. Signal.* 7 (2014) 1–7.
- [19] E.S. Lee, Z.G. Gao, Y.H. Bae, Recent progress in tumor pH targeting nanotechnology, *J. Control. Release* 132 (2008) 164–170.
- [20] Z.S. Ge, S.Y. Liu, Functional block copolymer assemblies responsive to tumor and intracellular microenvironments for site-specific drug delivery and enhanced imaging performance, *Chem. Soc. Rev.* 42 (2013) 7289–7325.
- [21] Z. Zhao, H. Meng, N. Wang, M.J. Donovan, T. Fu, M. You, Z. Chen, X. Zhang, W. Tan, A controlled-release nanocarrier with extracellular pH value driven tumor targeting and translocation for drug delivery, *Angew. Chem. Int. Ed. Engl.* 52 (2013) 7487–7491.
- [22] R. Mo, Q. Sun, N. Li, C. Zhang, Intracellular delivery and antitumor effects of pH-sensitive liposomes based on zwitterionic oligopeptide lipids, *Biomaterials* 34 (2013) 2773–2786.
- [23] M.-H. Lai, S. Lee, C.E. Smith, K. Kim, H. Kong, Tailoring polymersome bilayer permeability improves enhanced permeability and retention effect for bioimaging, *ACS Appl. Mater. Interfaces* 6 (2014) 10821–10829.
- [24] H. Nehoff, N.N. Parayath, L. Domanovitch, S. Taurin, K. Greish, Nanomedicine for drug targeting: strategies beyond the enhanced permeability and retention effect, *Int. J. Nanomedicine* 9 (2014) 2539.
- [25] D. Everett, Manual of symbols and terminology for physicochemical quantities and units, appendix II: definitions, terminology and symbols in colloid and surface chemistry, *Pure Appl. Chem.* 31 (1972) 577–638.
- [26] Z. Luo, K. Cai, Y. Hu, L. Zhao, P. Liu, L. Duan, W. Yang, Mesoporous silica nanoparticles end-capped with Collagen: redox-responsive nanoreservoirs for targeted drug delivery, *Angew. Chem. Int. Ed. Engl.* 50 (2011) 640–643.
- [27] S.-W. Song, K. Hidajat, S. Kawi, Functionalized SBA-15 materials as carriers for controlled drug delivery: influence of surface properties on matrix–drug interactions, *Langmuir* 21 (2005) 9568–9575.
- [28] Z.G. Yue, W. Wei, P.P. Lv, H. Yue, L.Y. Wang, Z.G. Su, G.H. Ma, Surface charge affects cellular uptake and intracellular trafficking of chitosan-based nanoparticles, *Biomacromolecules* 12 (2011) 2440–2446.
- [29] M. Koivusalo, C. Welch, H. Hayashi, C.C. Scott, M. Kim, T. Alexander, N. Touret, K.M. Hahn, S. Grinstein, Amiloride inhibits macropinocytosis by lowering submembranous pH and preventing Rac1 and Cdc42 signaling, *J. Cell Biol.* 188 (2010) 547–563.
- [30] I.H. Koumakpayi, C. Le Page, N. Delvoye, F. Saad, A.M. Mes-Masson, Macropinocytosis inhibitors and Arf6 regulate ErbB3 nuclear localization in prostate cancer cells, *Mol. Carcinog.* 50 (2011) 901–912.
- [31] M. Joglekar, S. Khandelwal, D.B. Cines, M. Poncz, L. Rauova, G.M. Arepally, Heparin enhances uptake of platelet factor 4/heparin complexes by monocytes and macrophages, *J. Thromb. Haemost.* 13 (2015) 1416–1467.
- [32] G. Vassiliou, R. McPherson, A novel efflux–recapture process underlies the mechanism of high-density lipoprotein cholesteryl ester-selective uptake mediated by the low-density lipoprotein receptor–related protein, *Arterioscler. Thromb. Vasc. Biol.* 24 (2004) 1669–1675.
- [33] H.R. Kim, S. Gil, K. Andrieux, V. Nicolas, M. Appel, H. Chacun, D. Desmaele, F. Taran, D. Georgin, P. Couvreur, Low-density lipoprotein receptor-mediated endocytosis of PEGylated nanoparticles in rat brain endothelial cells, *Cell. Mol. Life Sci.* 64 (2007) 356–364.
- [34] W. Zhang, J. Liu, Q. Zhang, X. Li, S. Yu, X. Yang, J. Kong, W. Pan, Enhanced cellular uptake and anti-proliferating effect of chitosan hydrochlorides modified genistein loaded NLC on human lens epithelial cells, *Int. J. Pharm.* 471 (2014) 118–126.
- [35] J.W. Perry, C.E. Wobus, Endocytosis of murine norovirus 1 into murine macrophages is dependent on dynamin II and cholesterol, *J. Virol.* 84 (2010) 6163–6176.
- [36] Y. Cai, E.N. Postnikova, J.G. Bernbaum, S. Yú, S. Mazur, N.M. Deilulis, S.R. Radoshitzky, M.G. Lackmeyer, A. McCluskey, P.J. Robinson, Simian hemorrhagic fever virus cell entry is dependent on CD163 and uses a clathrin-mediated endocytosis-like pathway, *J. Virol.* 89 (2015) 844–856.
- [37] S.B. Sieczkarski, G.R. Whittaker, Influenza virus can enter and infect cells in the absence of clathrin-mediated endocytosis, *J. Virol.* 76 (2002) 10455–10464.
- [38] G.R. Ares, P.A. Ortiz, Dynamin2, clathrin, and lipid rafts mediate endocytosis of the apical Na/K/2Cl cotransporter NKCC2 in thick ascending limbs, *J. Biol. Chem.* 287 (2012) 37824–37834.
- [39] J.A. Daniel, N. Chau, M.K. Abdel-Hamid, L. Hu, L. von Kleist, A. Whiting, S. Krishnan, P. Maamary, S.R. Joseph, F. Simpson, Phenothiazine-derived antipsychotic drugs inhibit dynamin and clathrin-mediated endocytosis, *Traffic* 16 (2015) 635–654.
- [40] Y. Yamada, R. Furukawa, Y. Yasuzaki, H. Harashima, Dual function MITO–porter, a nano carrier integrating both efficient cytoplasmic delivery and mitochondrial macromolecule delivery, *Mol. Ther.* 19 (2011) 1449–1456.
- [41] M. Longmire, P.L. Choyke, H. Kobayashi, Clearance properties of nano-sized particles and molecules as imaging agents: considerations and caveats, *Nanomedicine* 3 (2008) 703–717.
- [42] Y. He, H. Xu, S. Ma, P. Zhang, W. Huang, M. Kong, Fabrication of mesoporous spherical silica nanoparticles and effects of synthesis conditions on particle mesostructure, *Mater. Lett.* 131 (2014) 361–365.